Applied Mathematics & Information Sciences
An International Journal

http://dx.doi.org/10.18576/amis/190116

Development of Ultra-Wideband Planar Antenna to Detect Hematoma in the Human Brain

Mohanad A. Deif [1,*], *Hani Attar* [2,3], *Mohamed A. Hafez* [4], *Waleed Alomoush* [5] *and Hussein Al-Faiz* [6]

[1]Department of Artificial Intelligence, College of Information Technology, Misr University for Science & Technology (MUST), 6th of October City 12566, Egypt
[2]Faculty of Engineering, Zarqa University, Zarqa, Jordan
[3]College of Engineering, University of Business and Technology, Jeddah, 21448, Saudi Arabia
[4]Faculty of Engineering, FEQS, INTI -IU, Universi, Nilai, Malaysia
[5]School of Computing, Skyline University College, Sharjah, United Arab Emirates
[6]Institute of Power Engineering (IPE), Universiti Tenaga Nasional, Kajang, 43000, Malaysia

Received: 5 Jun. 2024, Revised: 28 Jul. 2024, Accepted: 28 Sep. 2024.
Published online: 1 Jan. 2025.

Abstract: Undetected intracranial injuries have the potential to lead to enduring cerebral impairments, significant functional limitations, or fatality. The timely diagnosis and treatment of intracranial hematomas is crucial to enhance patient outcomes. Magnetic Resonance Imaging (MRI) and Computed Tomography (CT) are medical imaging techniques utilized to identify and diagnose brain hemorrhage and malignancies. The proposed work aims to investigate the efficacy of Ultra-Wide Band (UWB) signals in detecting Hematoma within the cranial region of the human body. UWB technology possesses extensive capabilities in terms of speed and a remarkably low power density; moreover, it receives input signals within extremely short pulse durations ranging from 100 picoseconds to a few nanoseconds. As a result of this low power density, UWB does not cause ionization of tissues. The bandwidth exceeds 20% of the central frequency, which is equivalent to 500MHz. The average power spectral density must remain below -41.3 dBm/MHz within the frequency range of 3.1 to 10.6 GHz, as this range is commonly employed in medical applications. The skull model is comprised of seventeen distinct tissue types, namely: Sclera, Vitreous Humor, Eye Lens, Skin, Grey matter (GM), Cerebro-Spinal-Fluid (CSF), Dura, Fat, Cerebellum, Blood, Muscles, White matter (WM), Spinal Cord (nerve), Bone, Tongue, Cartilage, and Sinuses (air). The model assigns distinct dielectric characteristics (within the frequency range of 3.1 to 9 GHz) to each layer based on the corresponding tissue types. This study presents a proposed model with the objective of examining how intracranial hemorrhage affects the characteristics of ultra-wideband waves reflected and transmitted from a simulated brain model. The practical implementation of the phantom head model was accomplished through the utilization of CST MICROWAVE STUDIO software.

Keywords: CST, Brain, Hematoma, MRI image and UWB.

1 Introduction

The most applicable technique in most developing countries to identify brain hematoma contains the implementation of two main medical processes, where the first one is Computed Tomography (CT), and the second one is the Magnetic Resonance Imaging (MRI) [1]-[3].

Regrettably, several hospitals encounter limitations in their ability to implement CT and MRI technologies, most likely, as results of the large device installation spaces and the specific operational requirements.

Indeed, CT and MRI are huge in size and need to be installed and operated in a precise, correct, and specific way [4]. Additionally, considerable financial investment and the necessity for adequately trained personnel provide further challenges, mainly because the availability of qualified staff may not always be guaranteed. The lack of portability of MRI and CT technologies makes it impossible to transfer them to the operational location (accident place or client home for example), instead, patients are required to be transported to hospitals [5], [6], resulting in a critical delay in the treatment time, which may potentially lead to severe consequences, such as impairment or mortality. Hence, it is essential well-demanded to produce a non-intrusive and easily transportable CT and MRI systems [7],[8], where the systems would provide healthcare professionals with a tool that can be promptly employed on-site following in urgent care settings, an injury, and within in-home healthcare environments; consequently, reducing the delay in starting the treatment processes, which may include decisive medical involvement [8], leading to enhanced patient outcomes and decreased costs. Furthermore, the necessity for CT scans is reduced, as a result, the danger of undesired interaction with X-rays is mitigated [9].

*Corresponding author e-mail: Mohanad.Deif@must.edu.eg

© 2025 NSP
Natural Sciences Publishing Cor.

The proposed work in [10] utilized an Ultra-Wide Band (UWB) signal for the detection of hematomas within the human skull, which introduces the potential for implementing the aforementioned technology. In the year 1901, Guglielmo Marconi accomplished a noteworthy feat by employing UWB communications to successfully send sequences of Morse code crossing the Atlantic Ocean utilizing spark gap radio transmitters [11],[12]. Nevertheless, the potential benefits of Electro-Magnetic Pulses (EMPs), such as the wide bandwidth and ability to facilitate the advancement of multi-user systems, have yet to be well addressed in the discourse. As per the guidelines set forth by the Federal Communications Commission (FCC), it is mandated that UWB transmissions must exhibit a bandwidth that is either equal to or greater than 20% of the central frequency, or a minimum of 500MHz [13]. Based on the findings of references [14] and [15], it is advised to maintain the average power spectral density below -41.3 dB/MHz for medical purposes within the frequency range spanning from 3.1 to 10.6 GHz.

The utilization of UWB imaging technology allows clinicians to non-invasively monitor the movement of organs [16]. In juxtaposition to traditional ultrasound instruments that require direct contact with the skin, UWB sensors and imaging systems have the capability to operate from a certain distance [17]. Due to the non-ionizing nature, UWB signals do not elicit the adverse effects associated with X-ray instruments, such as CT scanners [18]. Clinicians have the ability to make an initial diagnosis applying UWB imaging that allows them to avoid subjecting patients to any potential risks or discomfort [19]. The extensive UWB frequency spectrum contains low frequencies characterized by long wavelengths, which allow UWB signals to efficiently penetrate various substances. As a result, UWB signals can typically pass through materials with low conductivity, such as skin, muscle, fat, and bone, but they encounter limitations when dealing with highly conductive materials like metals.

The focus of this study is the development of a diagnostic system that primarily utilizes an UWB signal for the detection of hematomas in the human head, accordingly, the human head model and the UWB mechanism are regarded as the main components for the investigated system. Consequently, computer software has been employed in creating and simulating the head of a human model, mainly due to the inherent difficulties associated with its biological structure. The simulation enables a safe evaluation of the system prior to conducting trials involving human subjects.

2 Preliminaries

This section presents medical information about the definition and discussion on brain hematoma due to their impact on human life, concept and applications of Ultra-wide band and finally explanation of the fundamental antenna theory.

2.1 Human Brain Hematoma

A hematoma is characterized as an accumulation or aggregation of blood. Skull fractures or shearing injuries have the potential to cause tearing of blood vessels in the cranial region, where Multiple types of Hematoma can occur. The formation of a hematoma can occur either immediately following a cranial trauma or subsequently. Hematomas have the potential to induce cerebral edema, intracranial hypertension, or a state of unconsciousness, moreover, the Hematoma may be surgically excised [20]. The outcome of a hematoma is contingent upon its location and whether it exhibits progressive enlargement or associated complications. Annually, a total of 2 million individuals in the United States need medical treatment for brain injuries. Out of the aforementioned figures, a total of 500,000 individuals are admitted to hospitals, 50,000 succumb to their conditions, and 90,000 experience enduring impairments [21]. Human Brain hematoma is usually categorized into three basic kinds: intracerebral Hematoma, epidural Hematoma and subdural Hematoma [22],[23]. It is illustrated in Fig. 1 and Fig. 2 that there are various classifications of hematomas depending on the anatomical locations where blood accumulates and CT scan Image. The details of brain hematoma types have been explained as the following:

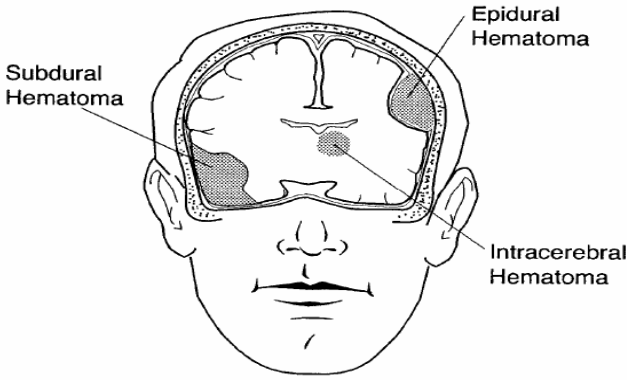

Fig. 1: Hematomas classifications.

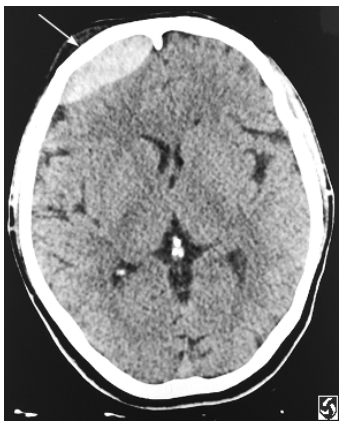

(a)

© 2025 NSP
Natural Sciences Publishing Cor.

(b)

(c)

Fig. 2: CT scan Image for a patient with (a) epidural Hematoma, (b) intracerebral Hematoma, (c) subdural Hematoma.

- *Epidural Hematoma*

The term "epidural" refers to a location situated above the dura mater, which is the outermost layer of the brain located amid the skull and the brain [24]-[26], where the dura mater is the resilient outermost layer that encloses the brain and situated among the cranium and the brain tissue, taking into consideration that the hemorrhaging occurs in the space between the dura mater and the cranium.

- *Subdural Hematoma*

A subdural hematoma is a pathological condition characterized by the collection of blood in the subdural space, which is located between the brain's outer surface and the dura mater and referred as the intracranial compartment, which is normally characterized by a restricted presence of cerebrospinal fluid that functions as a safeguarding and cushioning agent for the brain. The etiology of a subdural hematoma frequently involves traumatic events or vascular injury within the cranial compartment. The slow accumulation of blood within the body can occur without noticeable symptoms, leading to the formation of a thrombus that exerts pressure on the brain region. The aforementioned pressure has the potential to induce neurological manifestations such as headaches, cognitive dysfunction, and in severe cases,

loss of consciousness or fatality if not expeditiously attended. The degree of severity exhibited by a subdural hematoma may vary, hence requiring medical intervention, such as the implementation of surgical drainage. The diagnosis and management of subdural hematomas hold significant importance in the fields of neurosurgery and emergency care, as they require a comprehensive grasp of cerebral anatomy and involve potentially life-threatening consequences associated with bleeding in the subdural space.

- *Intracerebral Hematoma*

The term "intra" refers to the inside or internal aspect, whereas "cerebral" pertains to the brain, whereas intracerebral hemorrhage refers to the occurrence of bleeding within the brain tissue. The occurrence of a hematoma has the potential to induce cerebral edema, elevated intracranial pressure, or a state of coma. Diagnosis of brain hematoma [27],[28].

The present approach employed for the identification of brain hematoma involves the utilization of MRI and CT techniques, which unfortunately are not available in all healthcare centers as a result of the high cost of such highly advanced technologies. Moreover, the large spaces needed to fit CT and MRI make small healthcare centers out of such services. Besides the high cost and large size, CT and MRI require specialized personnel with appropriate qualifications to operate, adding extra change of implementation.

The importability of CT and MRI device forces patients to go to healthcare centers or hospitals, causing delay in treatment processes, which is potential to ultimately lead to the manifestation of impairment or mortality; therefore, the objective is to design and create a portable and non-invasive device, which would provide medical professionals with a readily available tool for usage in various contexts, including home healthcare, urgent care facilities, and the site of an injury environments. The utilization of such technology will effectively reduce superfluous delays prior to the implementation of the ultimate medical action. As a result, the needed small size and cheap MRI device will enhance patient outcomes and decrease the cost. Moreover, this device will limit the need for scans using CT, thus minimizing undue X-rays exposure. The mentioned system can be realized through the utilization of a UWB signal, which can proficiently identify hematomas within the human skull [29]-[31].

- *Scattering Matrix and Energy Transmission in Ultra-Wide Band*

The scattering matrix serves as a mathematical framework for quantifying the transmission of UWB energy, implementing UWB antennas [32]. In an N-port configuration, the S-matrix consists of N2 coefficients known as S-parameters, where the S-matrices for single-port,

© 2025 NSP
Natural Sciences Publishing Cor.

dual-port, and three-port antennas are:

$$\text{S-Matrix for single-port} = [S_{11}] \quad (1)$$

$$\text{S-Matrix for two-ports} = \begin{bmatrix} S_{11} & S_{12} \\ S_{21} & S_{22} \end{bmatrix} \quad (2)$$

$$\text{S-Matrix for three-ports} = \begin{bmatrix} S_{11} & S_{12} & S_{13} \\ S_{21} & S_{22} & S_{23} \\ S_{31} & S_{32} & S_{33} \end{bmatrix} \quad (3)$$

The S-parameters, denoted as "S" are defined by paired subscripts, "ij," where "i" represents the output port and "j" represents the source port (the input port), for example, S11 denotes the ratio of the reflected signal originating from port one to the incident signal on port one, whereas S12 pertains to the UWB signal transfer from port 1 to port 2.

This section presents medical information about the definition and discussion on brain hematoma due to their impact on human life, concept and applications of Ultra-wide band and finally explanation of the fundamental antenna theory.

The reflection coefficients (S11, S22, S33, …, etc.) of the scattering matrix correspond to the parameters along the diagonal and pertain to the behavior at a single port. On the other hand, the transmission coefficients, referred to as off-diagonal S-parameters, describe the behavior from one port to another.

The matrix and equation have identical numerical values. Equations (4), (5), and (6) provide the mathematical description of the two-port network, where "a" denotes the voltage at each port, and "b" the voltage exiting a given port [32]:

$$\begin{bmatrix} b_1 \\ b_2 \end{bmatrix} = \begin{bmatrix} S_{11} & S_{12} \\ S_{21} & S_{22} \end{bmatrix} \begin{bmatrix} a_1 \\ a_2 \end{bmatrix} \quad (4)$$

$$b_1 = S_{11}a_1 + S_{12}a_2 \quad (5)$$

$$b_1 = S_{21}a_1 + S_{22}a_2 \quad (6)$$

For the assessment of S11 and S21 coefficients, an input is introduced to port one with port 2 terminated. Subsequently, the output is gauged at ports 1 (S11) and ports 2 (S21) shown in Eq. (7) and Eq. (8). Similarly, the identical procedure is reiterated with the input administered to port two while port one is terminated, where the output measurement is then taken at port 1 (S12) and port 2 (S22) shown in Eq. (9) and Eq. (10):

$$S_{11} = \frac{b_1}{a_1}, where\ a_2 = 0 \quad (7)$$

$$S_{21} = \frac{b_2}{a_1}, where\ a_2 = 0 \quad (8)$$

$$S_{22} = \frac{b_1}{a_1}, where\ a_1 = 0 \quad (9)$$

$$S_{12} = \frac{b_1}{a_1}, where\ a_1 = 0 \quad (10)$$

Where S11 and S22 are the reflection coefficient at port 1 and 2, respectively, and S21 and S12 are the voltage transfer ratio for port 2 to port 1, and port 1 to port 2, respectively.

The UWB Antenna Design Specifications

The UWB antenna specifications have been documented in reference [33], as following:

1. The UWB antenna is required to function within the frequency range starting at 3.1 GHz to 10.6 GHz. Hence, in order to mitigate substantial return loss and matching issues, it is imperative for the impedance of the UWB antenna to encompass a bandwidth of 7.5 GHz.
2. The UWB antenna needs to demonstrate consistent linear phase characteristics throughout its frequency range and uphold a constant group delay within the designated frequency range. This requirement implies that the antenna should exhibit minimal pulse dispersion.
3. The desirability of an omnidirectional radiation pattern lies in its ability to facilitate user mobility and provide freedom in positioning the transmitter or receiver.
4. The radiation efficiency should be substantially increased due to the low transmit power spectral density. The Federal Communications Commission (FCC) has established an upper limit of -41dBm/MHz
5. The antenna must possess a physically small and low-profile design, ideally in a planar configuration. The ideal antenna dimensions should be relatively modest in comparison to the wavelength, and preferably lightweight. Additionally, it is desirable for the antenna to possess a compact and sturdy design.

3 Methodology

The process of generating a detailed human head model and conducting simulations of the UWB system are presented in this section, using the CST MICROWAVE STUDIO® software, version 5, which is a pivotal step in comprehending the way electromagnetic waves propagate through complex biological structures and evaluating the system's performance, whereas the subsequent section elucidates the simulation process conducted by the aforementioned software.

3.1 Human Head Modeling

The model employed in this study was crafted by means of anatomical representation; and it was constructed based on a dataset of MRI images, and hence provides an account of the head MRIs and delves extensively into the procedure of creating the model of the human head from the MRI data.

(1) Data Set for Magnetic Resonance Images

The model under consideration was constructed using MRI scans of the cranial region obtained from human participants at Emory University school of medicine [27]. The provided scans were acquired from a 23-year-old male with a body weight of 86 kg as most popular example in the investigated field. A high-resolution dataset consisting of 160 pictures

© 2025 NSP
Natural Sciences Publishing Cor.

was utilized for analysis. The imaging modality employed in this investigation is referred to as three-dimensional rapid low angle shot (3D-FLASH) MRI. The imaging parameters utilized in this study were as follows: a time to echo (TE) of 5 milliseconds, a repetition time TR of 35 milliseconds, a flip angle of 40 degrees, a total scan duration of 17 minutes, 1mm x 1mm x 1mm dimensions of each voxel, and the total volume of the cranium is partitioned into a matrix with dimensions of 256 × 256 x 160. Moreover, the photos acquired using the DICOM medical procedure for the human head model are transformed into grayscale. Fig. 3 depicts a representative subset of the MRI scans employed in the construction of the human head model.

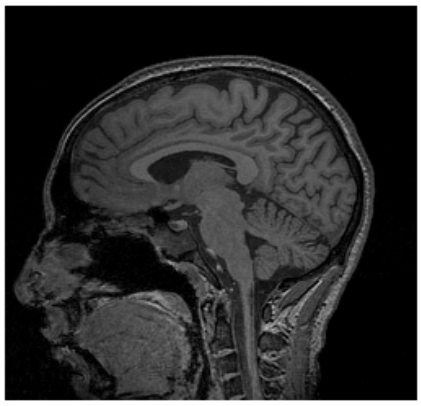

Fig. 3: The MRI image of the real human head.

The provided illustration depicts a mid-sagittal cross-sectional view of the anatomical structure of the head, as described in the cited source [34]. To obtain a more comprehensive understanding of the dielectric properties attributed to the human head model, it is recommended to return to reference [9].

The segmentation process involves applying a series of process steps to segment each of the 160 sagittal pictures, which are as following:

Step 1. Converting the MRI image to bitmap image for human head: The "EzDicom" software [35] is utilized to interpret each sagittal grayscale DICOM image with dimensions of 256 x 256. Subsequently, the image is converted into a grayscale bitmap format with dimensions of 256 × 256 pixels. The pixel size of the resultant bitmap image is 1mm x 1mm based on.

Step 2. Down-sampling the bitmap image for the human head: The 256 x 256 pixel-sized bitmap images, with each pixel measuring 1mm x 1mm [30], are processed using the "MATLAB" software. The 'imread' function is utilized to read these images, followed by a down sampling operation is applied to the 256 x 256 matrices, resulting in 128 x 128 matrices of the same data type, where the down sampling process is accomplished using the 'resizem' function in "MATLAB". Subsequently, the resized matrices (with the now dimensions of 128 × 128) are then converted back into bitmap images using the 'imwrite' function within the "MATLAB" software. This conversion alters the pixel size to 2mm x 2mm, as outlined in reference [36].

Step 3. Segmentation: The bitmap image with dimensions of 128 × 128 is afterwards accessed through the software application "MSPaint", afterwards, a manual segmentation process is undertaken to differentiate the various tissue types, with each kind being allocated a distinct color. Fig. 4 illustrates the segmented image obtained as a result of the applied segmentation procedure.

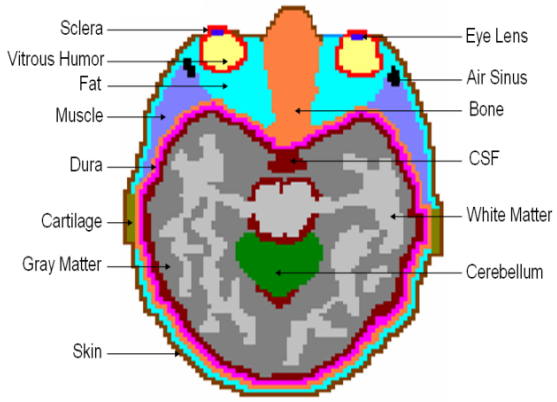

Fig. 4: The bitmap image for human head.

Step 4. Simulation for the model: Based on the outcome of the segmentation procedure, it was observed that the human head model exhibited seventeen distinct tissue types, namely: crystalline lens, dura mater, adipose tissue, spinal cord (nervous tissue), cutaneous tissue, grey matter, osseous tissue, white matter, vitreous humor, blood, cerebrospinal fluid (CSF), cerebellum, cartilage, lingual tissue, muscular tissue, sclera, and air-filled sinuses. The simulated human head model has been developed by the software package CST MICROWAVE STUDIO®. Fig. 5 presents a comprehensive flow chart outlining the sequential stages employed in the creation of the human head model.

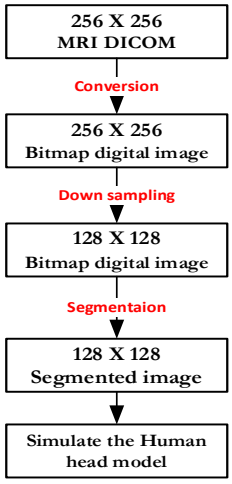

Fig. 5: Process steps flow-chart to simulate the presented Human head model.

© 2025 NSP
Natural Sciences Publishing Cor.

3.2 Ultra-Wide Band (UWB) antenna simulation and Structure

In this study, the antenna was enveloped by a layer simulating the structure of the human brain. In order to achieve the desired objective, a planar monopole with Compact Coplanar Waveguide (CPW) feeding; A feeding technique for microstrip antenna where the signal and ground currents are etched on the same layer [37]-[39] and circular patch utilizing UWB technology, was suggested as a potential choice for the implementation of this direct optimization strategy, where the aforementioned antenna has a very condensed configuration and a radiation pattern that covers all directions, and wide-ranging properties in unobstructed space [40]-[41].

The dielectric substrate selected for this study is the Rogers 4003, which possesses a relative permittivity of 3.28 and a thickness of 0.813 mm. In order to preserve the inherent attributes of these types of antennas, various optimization strategies were taken into account. Extensive research was conducted on the curvature of the ground plane with the objective of maintaining an omnidirectional radiation pattern that effectively penetrates human muscle tissue. Moreover, a deliberate selection was made to establish a distinct separation between the patch and the ground plane, with the intention of expanding the bandwidth (L_b = 1 mm). Furthermore, the patch exhibited an elliptical shape, which served the purpose of increasing the bandwidth, as opposed to the approach described in reference [42]. Fig. 6 and Table 1 illustrate the remaining dimensions of the antenna.

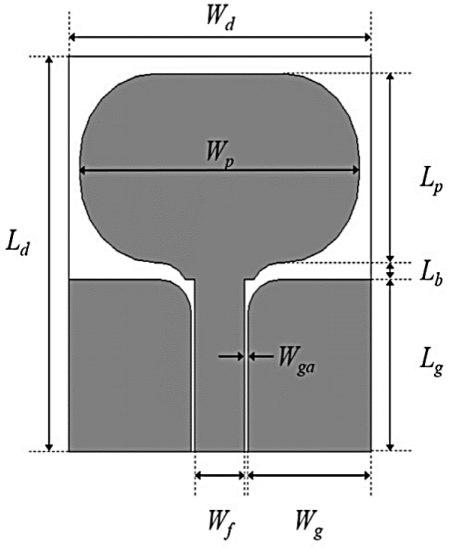

Fig. 6: Planar antenna Structure.

Table 1: UWB planar antenna dimensions.

Dimension name	Dimension Value (mm)
L_d	23
W_d	20
W_f	3.25
W_{ga}	0.25
L_p	11
W_p	18.5
L_g	10
W_g	4.5

As previously noted, the antenna is compact, allowing for an augmentation in the quantity of antennas encircling the head to evaluate the impact of multiple antennas on the outcomes.

3.3 Method of Detecting the Disease

The detection of intracranial bleeding involves the next four stages:

Stage one. Collection of Data:

After running the simulation, the S-parameters (which encompass S_{11}, S_{12}, S_{21}, S_{22}, …, etc.) are computed and gathered for further examination in the subsequent phases. The transmission and reflection coefficients are pivotal in determining the attributes of electromagnetic wave propagation through diverse human tissues.

Stage two. Calculations of The Variation Factor (VF):

The Variation Factor (VF) is utilized for the identification of any irregularity resulting from intracranial hemorrhage, as specified in Eq.(11):

$$\boldsymbol{VF} = \sqrt{\frac{d_1^2 + d_2^2 + \ldots\ldots\ldots\ldots + d_n^2}{n}} \quad (11)$$

The variable "d_i" represents the discrepancy between the established standard value and the observed abnormal value for the i-th sample, where i ranges from 1 to n, where "n" represents the overall count of samples, which we will set as 6000.

Stage three. Study of the reflection coefficients: During this stage, a comparison is made between the antenna reflection coefficients obtained from normal and abnormal cases utilizing the VF based on the existing idea on the symmetry of brain hemispheres, the present study involves a comparison of the VF for the reflection coefficients of two opposing UWB antennas located in the right and left hemispheres.

Consequently, the determination of whether the anomaly is located in the right or left hemisphere enables the estimation of the precise location of the cerebral hemorrhage.

Stage four. Study of Transmission coefficients: Following the identification of the major site of the internal hemorrhage in the previous stage, the VF is utilized to assess the transmission coefficients between the antenna in close proximity to the anomaly and its adjacent antennas. This comparison is conducted to validate the existence of abnormality and accurately ascertain its precise position.

© 2025 NSP
Natural Sciences Publishing Cor.

3.4 Experiments setup

UWB antennas are strategically positioned around the human head model at a fixed distance, denoted by D, which is equivalent to 2cm, where it is observed that if D is less than 2cm, the resulting signal response tends to be comparatively weaker in comparison to standard scenarios. The illustration in Fig. 7 displays the arrangement of these planar antennas.

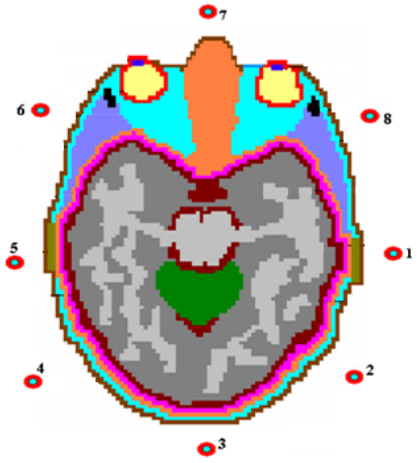

Fig. 7: Human head with eight antennas.

In this paper, a proposed model is introduced with the goal of analyzing the type of Hematoma, a type of internal brain hemorrhage, affects the transmission and reflection coefficients in the extremely wide frequency band. Through a series of experimental examinations, this study investigates the location, depth, and size affecting patients:

3.4.1 Cases of Brain Hematoma Detection

In this sub-section, two cases are investigated, as following:

Case 1: An elliptical Hematoma in Dura Matter:

The proposed Hematoma is an elliptical hematoma with dimensions 10 x 10 mm and thickness 2mm is inserted in head model in the layer of the Dura matter (Subdural Hematoma). Eight antennas are implemented, where the proposed position of this Hematoma between the first and the second antennas and close to the second antenna as shown in Fig. 8 as an example.

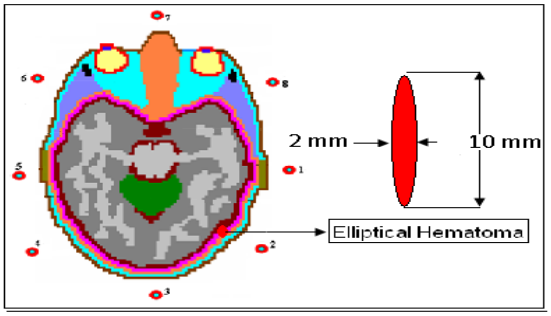

Fig. 8: Human head model with eight antennas and elliptical Subdural Hematoma

Case 2: An Elliptical Hematoma in Dura Matter Using 16 antennas:

In this case, case 1 is repeated but with increasing the number of antennas to sixteen antennas instead of eight, as shown in Fig. 9.

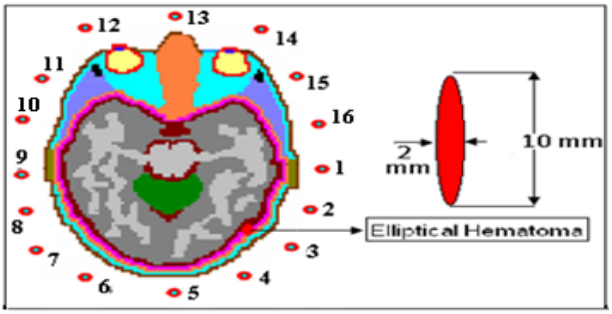

Fig. 9: Human head model with sixteen antennas and elliptical Subdural Hematoma.

4 Results and Discussion

This section shows the results obtained from various experiments explained in section 3.4 to show the effect of the Hematoma on the transmission and the reflection coefficients in the ultrawideband frequency range to distinguish between normal and abnormal cases.

4.1 Simulation of Planar Antenna

The gain pattern in the XZ-plane is simulated in CST and displayed in Fig. 2. The simulations were carried out using the theoretical permittivity values for human muscle tissue that were given in [9]. The antenna demonstrates a quasi-omnidirectional radiation pattern within the XZ. plane operating at UWB frequencies, as illustrated in. Thus, through the utilization of the mentioned downsizing procedure, it becomes feasible to confirm that the antenna can sustain an omnidirectional radiation pattern at UWB frequencies.

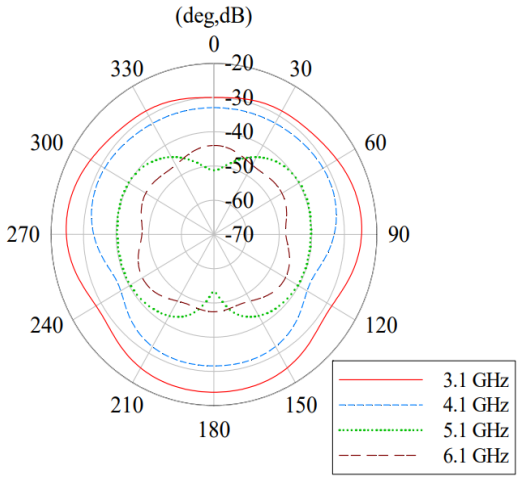

Fig. 10: Gain pattern of the planar antenna at 3.1, 4.1, 5.1 and 6.1 GHz.

© 2025 NSP
Natural Sciences Publishing Cor.

4.2 Cases of Brain Hematoma Detection

In this section, two cases are investigated, and the results are shown below:

Case 1: An elliptical Hematoma in Dura Matter:

The following figures show the reflection coefficients for all ports normal and abnormal cases. S_{11}, S_{22}, S_{33}, S_{44}, S_{55}, S_{66}, S_{77} and S_{88} are shown in Fig. 11.

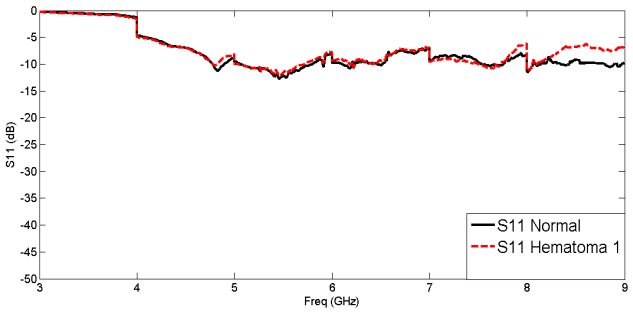

Port 1

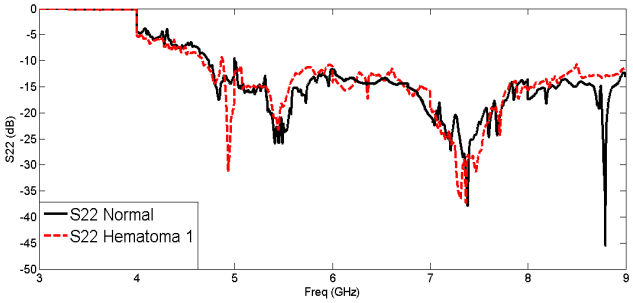

Port 2

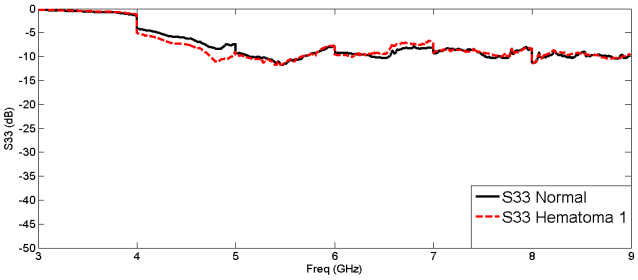

Port 3

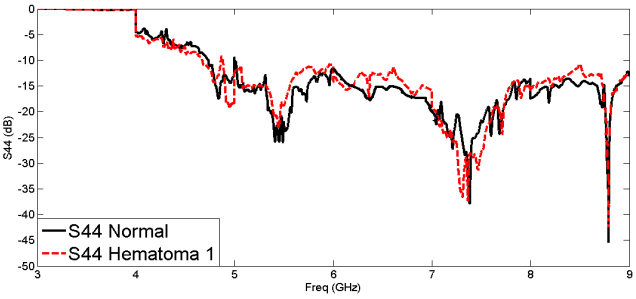

Port 4

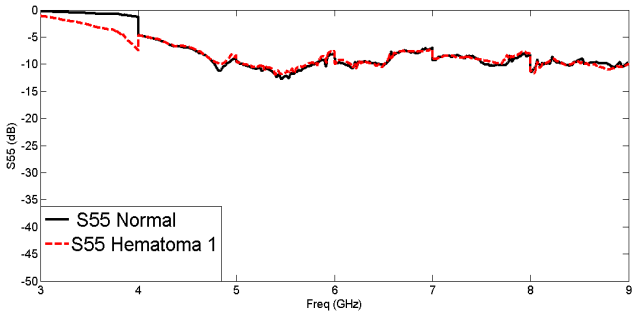

Port 5

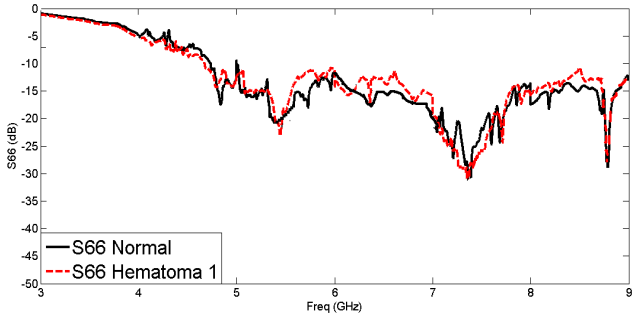

Port 6

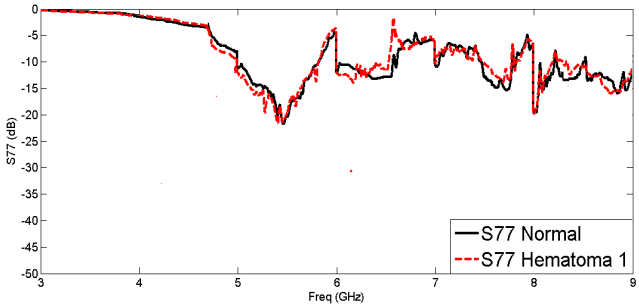

Port 7

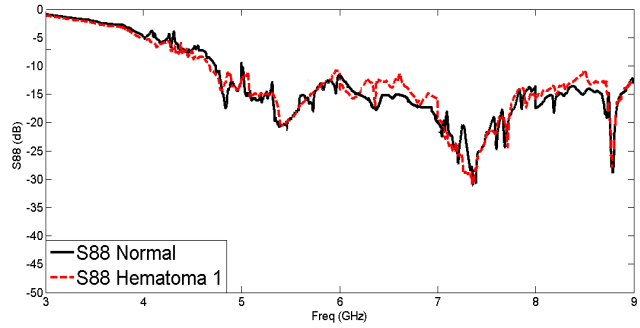

Port 8

Fig. 11: The reflection coefficients for all ports in case 1 with frequency range from 3 GHz – 9 GHz

By calculating the **VF** for the reflection coefficients of all UWB antennas (S_{11}, S_{22}, S_{33}, … S_{88}) as shown in Table 2. The effect of Hematoma on the value of **VF** helps us to expect the place of the Hematoma in the human head.

© 2025 NSP
Natural Sciences Publishing Cor.

Table 2: The VF for the reflection coefficients of case 1.

S-parameter	VF
S_{11}	1.062854
S_{22}	7.917066
S_{33}	0.724546
S_{44}	2.013141
S_{55}	1.03493
S_{66}	1.643377
S_{77}	0.523641
S_{88}	0.556248

From the obtained results, there is little VF for S_{11}, S_{33}, S_{44}, S_{55}, S_{66}, S_{77}, and S_{88} but the value increases for S_{22}, which means the bleeding occurs near antenna number two.

From the previous phase, it is noticed that the bleeding occurs near the second antenna as expected. Now the transmission coefficient between second antenna and first antenna, and between second antenna and third antenna will be used to predict the exact hematoma position. S_{21} ($S_{12} = S_{21}$) is shown in Fig. 12, where S_{23} is shown in Fig. 13., and the VFs are shown in Table 3.

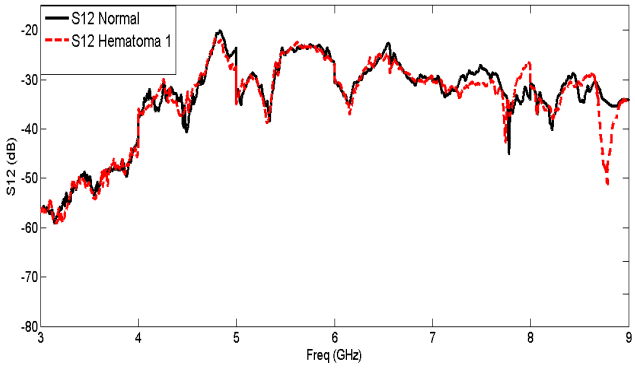

Fig. 12: S12 for case 1 in frequency range from 3 GHz – 9 GHz.

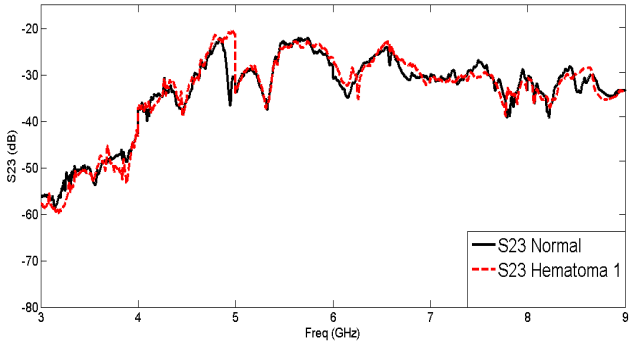

Fig. 13: S23 for case 1 in frequency range from 3 GHz – 9GHz.

Table 3: The VF for the transmission coefficients of case 1.

S-parameter	VF
S_{12}	1.462286
S_{23}	0.45909

From the results obtained, the value of the VF for S_{23} is smaller than the value of the VF for S_{12}, which means that exact hematoma position occurs between antenna number two and antenna number one.

Case 2: An Elliptical Hematoma in Dura Matter Using 16 antennas:

The Reflection coefficient of S_{11}, S_{22}, S_{33}, S_{44}, S_{55}, S_{66}, S_{77} , S_{88},S_{99}, S_{1010}, S_{1111}, S_{1212}, S_{1313}, S_{1414}, S_{1515}, and S_{1616} are shown in Fig. 14 .

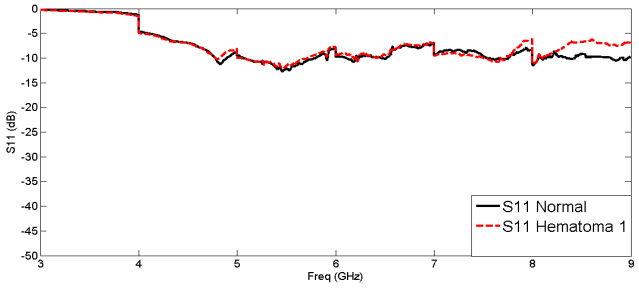

(a) Port 1

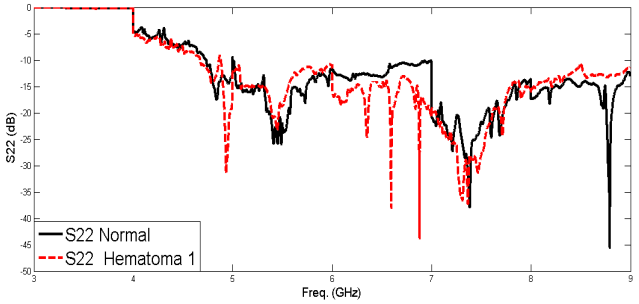

(b) Port 2

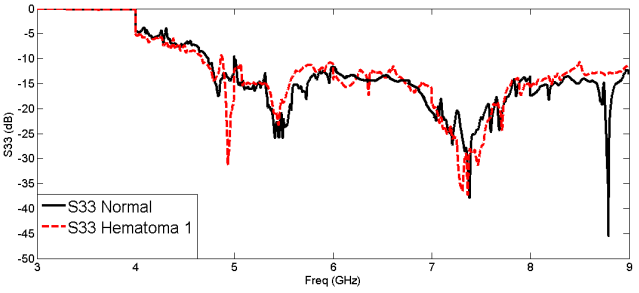

(c) Port 3

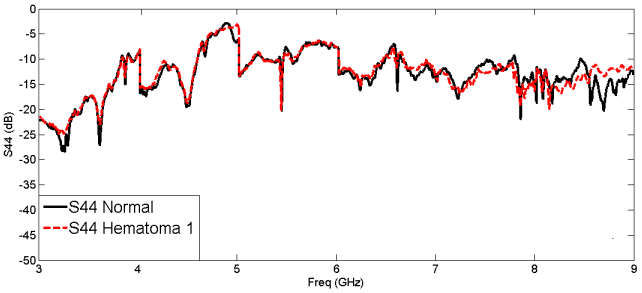

(d) Port 4

© 2025 NSP
Natural Sciences Publishing Cor.

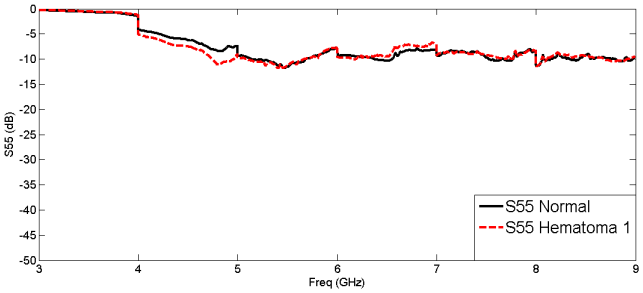

(e) Port 5

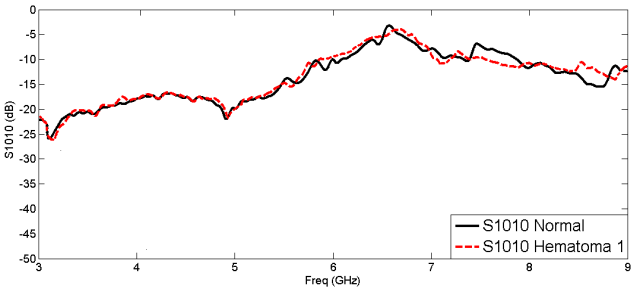

(j) Port 10

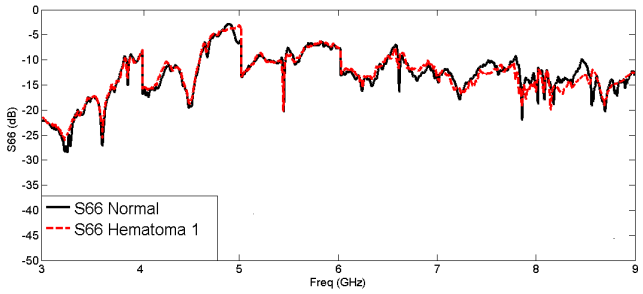

(f) Port 6

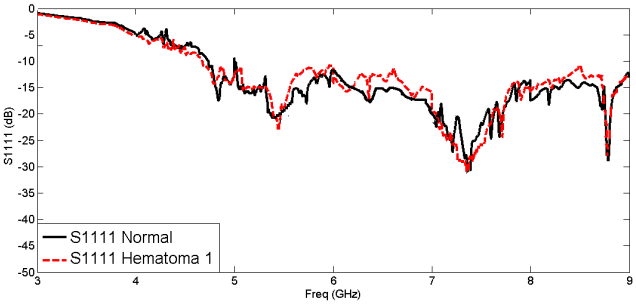

(k) Port 11

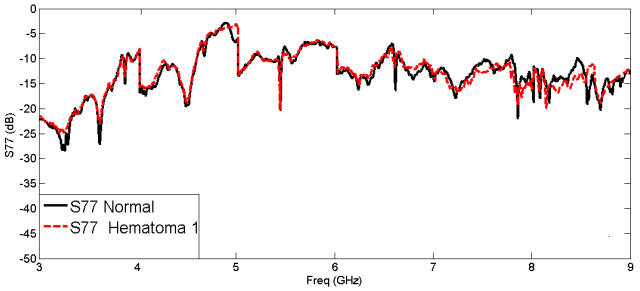

(g) Port 7

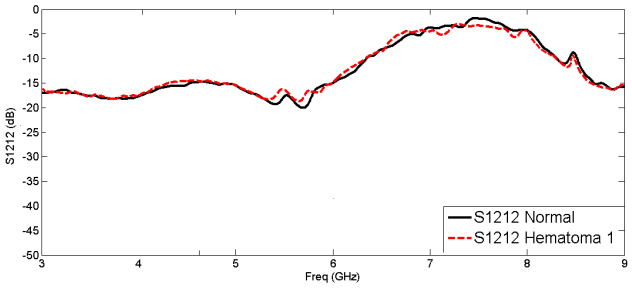

(l) Port 12

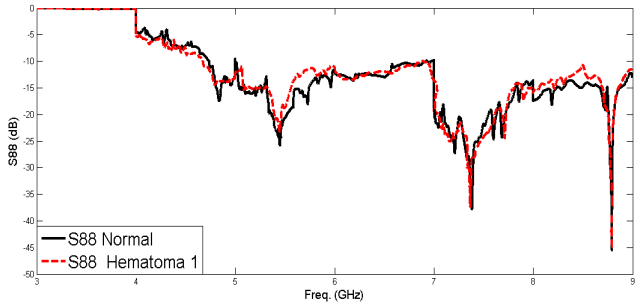

(h) Port 8

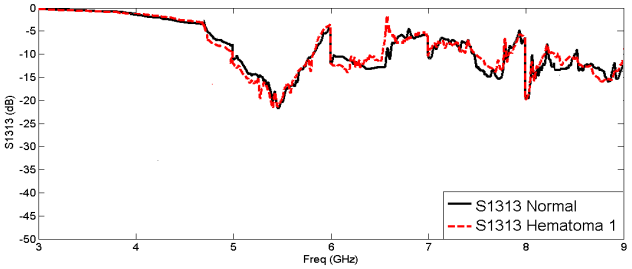

(m) Port 13

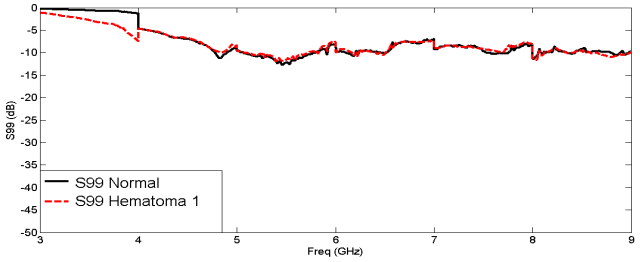

(i) Port 9

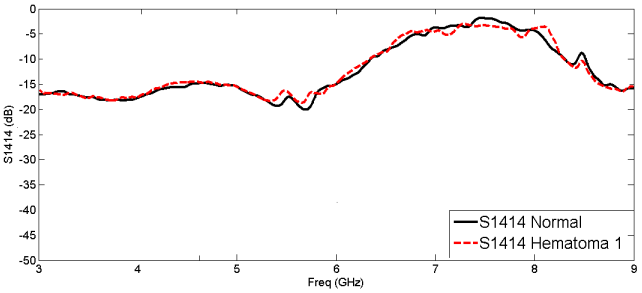

(n) Port 14

© 2025 NSP
Natural Sciences Publishing Cor.

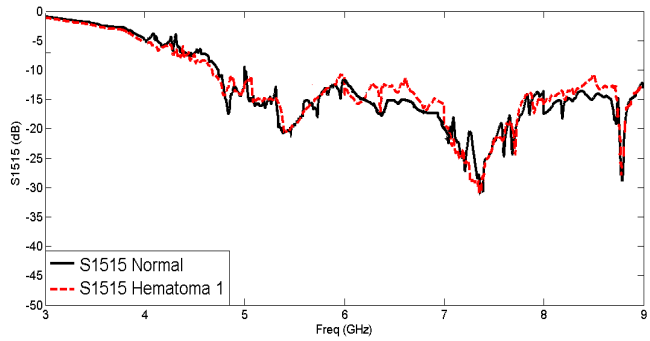

(o) Port 15

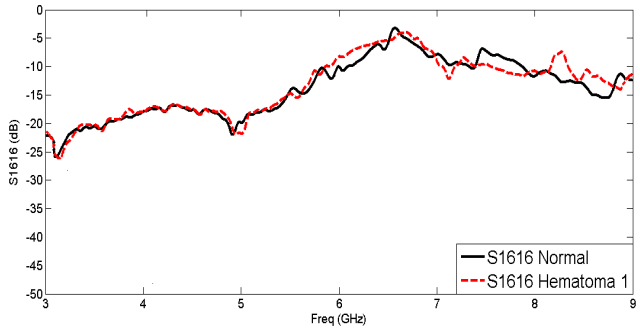

(p) Port 16

Fig. 14: The reflection coefficients for all ports in case 2 with frequency range from 3 GHz – 9 GHz.

By calculating the **VF** for the reflection coefficients of all antennas (S_{11}, S_{22}, S_{33}, ... S_{1515}), as detailed in Table 4, we can analyze the impact of Hematoma on the VF's values. This analysis aids us in predicting the location of the Hematoma within the human head.

Table 4: The VF for the reflection coefficients of case 2.

S-parameter	VF
S_{11}	1.062854
S_{22}	11.917066
S_{33}	7.917066
S_{44}	2.013141
S_{55}	1.03493
S_{66}	1.643377
S_{77}	0.523641
S_{88}	0.556248
S_{99}	1.542319
S_{1010}	0.39897
S_{1111}	0.52988
S_{1212}	0.81181
S_{1313}	0.59019
S_{1414}	0.39817
S_{1515}	0.57293
S_{1616}	0.72315

From the obtained results, there is little VF for S_{11}, S_{44}, S_{55}, S_{66}, S_{77}, S_{88}, S_{99}, S_{1010}, S_{1111}, S_{1212}, S_{1313}, S_{1414}, S_{1515}, and S_{1616} but the values of S_{22} and S_{33} increase, which means that the bleeding occurs near antenna number two.

From the previous phase, it is noticed that the bleeding occurs near the second antenna as expected, then the transmission coefficient between second antenna and first antenna, and between second antenna and third antenna are studied. The Transmission coefficient of S_{12}, and S_{23} are shown in Fig. 15 and Fig. 16, respectively

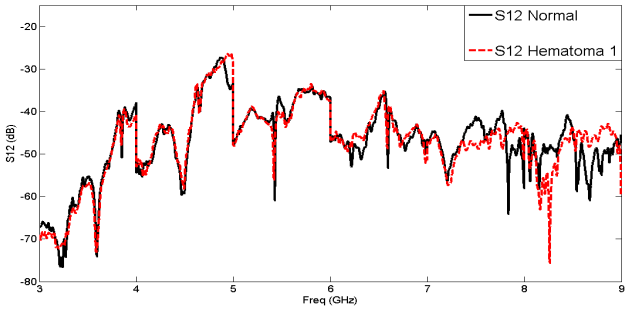

Fig. 15: S12 for case 2 in frequency range from 3 GHz – 9 GHz.

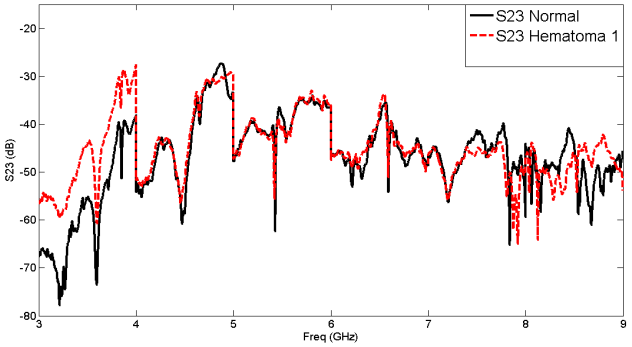

Fig. 16: S23 for case 2 in frequency range from 3 GHz – 9 GHz.

The VFs for S_{12} and S_{23} are shown in Table 5, where the results show the VF for S_{12} is smaller than S_{23}, which means that the Hematoma occurs between the second and the third antennas.

Table 5: The VF for the transmission coefficients of case 2.

S-parameter	VF
S_{12}	3.669931
S_{23}	5.63716

From the previous experience obtained, there are large variations (difference) between the normal and abnormal cases in reflection and transmission coefficients. This variation tends to be most pronounced in the nearest antenna to the site of injury, therefore, as increasing the number of UWB antennas surrounding the head model, the distances between them decrease, as depicted in Fig. 9. Consequently, the expansion in the number of antennas effectively covers nearly the entire area of the head, enhancing the UWB system's capability to detect even small volumes of Hematoma that may occur anywhere within the brain.

© 2025 NSP
Natural Sciences Publishing Cor.

5 Conclusion

In conclusion, this study has demonstrated the effectiveness of employing Ultra-Wide-Band (UWB) radar for the detection and identification of intracranial hemorrhage in the human cranium. A robust framework has been built by integrating a simulation model of the human head, utilizing the Finite Integration Technique (FIT) in computer software, and deploying small planar antennas, where eight-element and sixteen-element antennas are implemented. The methodology showcases the potential to rapidly and precisely detect occurrences of internal hemorrhaging in areas such as the Dura matter, gray matter, and white matter through the examination of the variability factor linked to each situation.

The importance of this approach is in its capacity to facilitate timely identification of brain hematoma, a crucial element in the management of human disease prior to its advancement to critical phases, which pose greater difficulties for treatment. The inclusion of an increased number of antennas surrounding the model of the human head enables more accurate localization of the Hematoma's position, hence substantially boosting the diagnostic accuracy of the procedure.

Given the significant progress made by this research, it is recommended that future investigations explore the following avenues:

1) Broadening the parameters to ascertain the dimensions and exact positioning of cerebral hematomas.
2) The development of technological advancements to facilitate the visualization of intracranial hemorrhage in the human cranium.
3) This study investigates the creation of a comparable circuit model for the established head model, providing a practical approach to accurately identifying the sites of brain hematomas.

In summary, this research makes a substantial contribution to the field of medical diagnostics by presenting a comprehensive framework for the timely identification and precise localization of brain hematomas. The potential influence of this intervention on improving patient care and treatment strategies is significant, and the opportunities for additional investigation offer promising prospects for refining and expanding these skills. Finally, it is important to mention that the proposed technique is much cheaper than the traditional ones and requires much smaller size, which makes it recommended to be implemented small healthcare centers and even in ambulance cars.

Funding

This work was funded in part by [INTI-IU-Malaysia] grant number [INTI-FEQS-01-06-20023].

Institutional Review Board Statement

Not applicable.

Data Availability Statement

Not applicable.

Conflicts of Interest

The authors declare no conflict of interest.

References

[1] E. Giampietri, D. Brizi, A. Monorchio, and N. Fontana, “Miniaturized antennas design for microwave imaging applications,” in 2020 IEEE International Symposium on Antennas and Propagation and North American Radio Science Meeting, IEEE, 2020, pp. 537–538.

[2] Attar, H., Ahmed, T., Rabie, R., Amer, A., Khosravi, M. R., Solyman, A., & Deif, M. A. (2024). Modeling and computational fluid dynamics simulation of blood flow behavior based on MRI and CT for Atherosclerosis in Carotid Artery. *Multimedia Tools and Applications*, *83*(19), 56369-56390.

[3] J. R. Petrella et al., “Preoperative functional MR imaging localization of language and motor areas: effect on therapeutic decision making in patients with potentially resectable brain tumors,” Radiology, vol. 240, no. 3, pp. 793–802, 2006.

[4] N. Baghdadi, A. S. Maklad, A. Malki, and M. A. Deif, “Reliable Sarcoidosis Detection Using Chest X-rays with EfficientNets and Stain-Normalization Techniques,” Sensors, vol. 22, no. 10, p. 3846, 2022.

[5] A. Pfuntner, L. M. Wier, and C. Stocks, “Most frequent conditions in US hospitals, 2011: statistical brief\# 162,” 2013.

[6] Attar, H., Solyman, A., Sayed, R. A., Mohamed, D. M., Hafez, M., & Deif, M. A. (2023, December). Improving Emergency Departments: Simulation-Based Optimization of Patients Waiting Time and the Number of Staff Present in A Hospital. In 2023 2nd International Engineering Conference on Electrical, Energy, and Artificial Intelligence (EICEEAI) (pp. 1-7). IEEE.

[7] J. Hsieh and T. Flohr, “Computed tomography recent history and future perspectives,” Journal of Medical Imaging, vol. 8, no. 5, p. 52109, 2021.

[8] C. L. Dunne et al., “A systematic review of interventions to reduce computed tomography usage in the emergency department,” Ann Emerg Med, 2022.

[9] K. Hashimoto, Y. Arai, K. Iwai, M. Araki, S. Kawashima, and M. Terakado, “A comparison of a new limited cone beam computed tomography machine for dental use with a multidetector row helical CT machine,” Oral Surgery, Oral Medicine, Oral

© 2025 NSP
Natural Sciences Publishing Cor.

Pathology, Oral Radiology, and Endodontology, vol. 95, no. 3, pp. 371–377, 2003.

[10] M. A. Saeed, M. Ahmad, A. Nwajana, M. U. Rehman, M. A. Sohaib, and A. Naseer, "Coaxial feed ultra-wideband microstrip antenna for medical applications," in 2022 International Conference on Electrical, Computer and Energy Technologies (ICECET), 2022, pp. 1–4.

[11] T. Lauteslager, M. Tømmer, T. S. Lande, and T. G. Constandinou, "Dynamic Microwave Imaging of the Cardiovascular System Using Ultra-Wideband Radar-on-Chip Devices," IEEE Trans Biomed Eng, vol. 69, no. 9, pp. 2935–2946, 2022.

[12] N. G. Gunaseelan, M. Anbarasan, V. A. Velvizhi, K. Jeyapiriya, and S. Gayathri, "Design of Microwave 3-D Antenna for Brain Tumour Sensing System," in 2022 International Conference on Communication, Computing and Internet of Things (IC3IoT), 2022, pp. 1–4.

[13] X. Yan, P. Gao, M. Cai, and Z. Li, "Simulation Research on Forward Problem of Magnetoacoustic Concentration Tomograghy of Magnetic Nanoparticles with Magnetic Induction Based on Multi-Coils," Progress In Electromagnetics Research Progress In Electromagnetics Research M, vol. 104, pp. 223–233, 2021.

[14] C. Sneka, A. Shuhaina, B. Vidhya, and others, "Design of Microstrip Patch Antenna for Brain Tumor Detection," in 2022 3rd International Conference on Electronics and Sustainable Communication Systems (ICESC), 2022, pp. 379–385.

[15] J. Vijayalakshmi and V. Dinesh, "Design of Compact Ultra-Wideband (UWB) Antennas for Microwave Imaging Applications," Next-Generation Antennas: Advances and Challenges, pp. 221–249, 2021.

[16] M. S. Talukder et al., "Rectangular slot with inner circular ring patch and partial ground plane based broadband monopole low SAR patch antenna for head imaging applications," Chinese Journal of Physics, vol. 77, pp. 250–268, 2022.

[17] S. Ali, Assessing the Viability of Wideband Transmission of Pulse Width Encoded Data Over an Inductive Link for Wireless Neural Implants. University of Toronto (Canada), 2020.

[18] K. Thakur, M. Sharma, M. Yadav, B. Singh, and others, "Ultra-Wide Band Antenna Design for Bio-Medical Application," International Journal of Research in Engineering, Science and Management, vol. 5, no. 5, pp. 72–74, 2022.

[19] R. Mishra, P. Kuchhal, and A. Kapoor, "Compact Multi-slotted Printed Antenna for Ultra-Wideband Applications in Medical Telemetry," IETE J Res, pp. 1–8, 2022.

[20] A. Alqerem, H. Attar, W. Alomoush, and M. Deif, "The Ability of Ultra Wideband to Differentiate Between Hematoma and Tumor Occur in The Brain," in 2022 International Engineering Conference on Electrical, Energy, and Artificial Intelligence (EICEEAI), IEEE, 2022, pp. 1–7.

[21] K. Üçel, "Design of a dual polarized low profile antenna for microwave brain imaging," Middle East Technical University, 2022.

[22] W. Alamro, B.-C. Seet, L. Wang, and P. Parthiban, "Early-Stage lung tumor detection based on Super-Wideband microwave reflectometry," Electronics (Basel), vol. 12, no. 1, p. 36, 2022.

[23] W. Wang, D. Yang, and Y. Lu, "Modeling and Simulation of Artery Occlusion for Early Detection of Carotid Atherosclerosis," in 2020 Chinese Control And Decision Conference (CCDC), 2020, pp. 4948–4952.

[24] Y. Tarek, R. Elgohary, and M. Deif, "Brain Tumor Detection Using GLCM and Machine learning Techniques," International Integrated Intelligent Systems, vol. 1, no. 2, 2024.

[25] J. Xue, Y. Wu, Y. Shi, and S. Cheng, "Brain storm optimization algorithm for multi-objective optimization problems," in Advances in Swarm Intelligence: Third International Conference, ICSI 2012, Shenzhen, China, June 17-20, 2012 Proceedings, Part I 3, 2012, pp. 513–519.

[26] P. Bhardwaj and R. K. Badhai, "Compact wideband folded strip monopole antenna for brain stroke detection," Int J Microw Wirel Technol, vol. 13, no. 9, pp. 937–946, 2021.

[27] M. Salimitorkamani, M. Mehranpour, and H. Odabasi, "A Miniaturized Wide-Band Sinuous Antenna for Microwave Brain Imaging Systems," IEEE Trans Antennas Propag, 2024.

[28] B. Li, H. Liu, Z. Zhang, and X. Gao, "A Rapid Microwave Imaging Approach for the Diagnosis of Traumatic Brain Injury.," Progress In Electromagnetics Research M, vol. 104, 2021.

[29] K. Shambavi and Z. C. Alex, "Printed dipole antenna with band rejection characteristics for UWB applications," IEEE Antennas Wirel Propag Lett, vol. 9, pp. 1029–1032, 2010.

[30] D. Awan, S. Bashir, S. Khan, S. S. Al-Bawri, and M. Dalarsson, "UWB Antenna with Enhanced Directivity for Applications in Microwave Medical Imaging," Sensors, vol. 24, no. 4, p. 1315, 2024.

[31] J. R. Kelly, P. S. Hall, and P. Gardner, "Band-notched UWB antenna incorporating a microstrip open-loop resonator," IEEE Trans Antennas Propag, vol. 59, no. 8, pp. 3045–3048, 2011.

[32] M. Yousaf et al., "An ultra-miniaturized antenna with

© 2025 NSP
Natural Sciences Publishing Cor.

ultra-wide bandwidth characteristics for medical implant systems," IEEE Access, vol. 9, pp. 40086–40097, 2021.

[33] A. H. Alghanimi, "Medical Application of Ultra-Wideband Technology," Innovations in Ultra-Wideband Technologies, 2021.

[34] [S. S. Hossain et al., "Image-based patient-specific flow simulations are consistent with stroke in pediatric cerebrovascular disease," Biomech Model Mechanobiol, vol. 20, pp. 2071–2084, 2021.

[35] H. Attar et al., "Modeling and computational fluid dynamics simulation of blood flow behavior based on MRI and CT for Atherosclerosis in Carotid Artery," Multimed Tools Appl, vol. 83, no. 19, pp. 56369–56390, 2024.

[36] V. Belov, M. Procofiev, T. Komandresova, and A. Samarkin, "Modification of the Minimal Bergman Model of the" Insulin-Glucose" System and its Implementation in MatLab/Simulink," in ENVIRONMENT. TECHNOLOGIES. RESOURCES. Proceedings of the International Scientific and Practical Conference, 2021, pp. 28–37.

[37] L. Yang et al., "Review on wearable antenna design," in International Conference in Communications, Signal Processing, and Systems, Springer, 2020, pp. 731–742.

[38] Z. Zhang and H. Liu, "Study on Ultra-wideband Multiple Differential Recursive Imaging of stroke: A recursive brain imaging solution for stroke detection.," in Proceedings of the 7th International Conference on Bioinformatics Research and Applications, 2020, pp. 34–38.

[39] M. A. Islam and J. L. Volakis, "A Reciprocity Based Deep Tissue Imaging Method Using On-body Microwave Sensors".

[40] S. Sasada et al., "Microwave breast imaging using rotational bistatic impulse radar for the detection of breast cancer: Protocol for a prospective diagnostic study," JMIR Res Protoc, vol. 9, no. 10, p. e17524, 2020.

[41] N. Abdullah and M. Z. A. A. Aziz, "Design of a High Directive Sensor With SRR for Microwave Imaging Application," in 2021 IEEE Asia-Pacific Conference on Applied Electromagnetics (APACE), IEEE, 2021, pp. 1–6.

[42] R. Ullah, I. Saied, and T. Arslan, "Measurement of whole-brain atrophy progression using microwave signal analysis," Biomed Signal Process Control, vol. 71, p. 103083, 2022.

© 2025 NSP
Natural Sciences Publishing Cor.